WILEY-VCH

DOI: 10.1002/ ((please add manuscript number))
Article type: Full Paper

Spatially-Resolved Insight into the Chemical and Electronic Structure of Solution Processed Perovskites – Why to (Not) Worry about Pin-Holes

Claudia Hartmann, Golnaz Sadoughi, Roberto Félix, Evelyn Handick, Hagen W. Klemm, Gina Peschel, Ewa Madej, Alexander B. Fuhrich, Xiaxia Liao, Simone Raoux, Daniel Abou-Ras, Dan Wargulski, Thomas Schmidt, Regan G. Wilks, Henry Snaith, and Marcus Bär**

C. Hartmann, Dr. R. Félix, E. Handick, Dr. X. Liao, Dr. D. Abou-Ras, D. Wargulski, Dr. R. G. Wilks, Prof. M. Bär
Renewable Energy
Helmholtz-Zentrum Berlin für Materialien und Energie GmbH
14109 Berlin, Germany
Email: claudia.hartmann@helmholtz-berlin.de; marcus.baer@helmholtz-berlin.de

Dr. G. Sadoughi, Prof. H. Snaith
Department of Physics, Clarendon Laboratory
University of Oxford
OX1 3PU, United Kingdom

H. W. Klemm, G. Peschel, Dr. E. Madej, A. B. Fuhrich, Dr. Th. Schmidt
Department of Chemical Physics – Spectro-Microscopy Group
Fritz-Haber-Institute of the Max-Planck-Society
14195 Berlin, Germany

Prof. S. Raoux, Dr. R. G. Wilks, Prof. M. Bär
Energy Materials In-Situ Laboratory (EMIL)
Helmholtz-Zentrum Berlin für Materialien und Energie GmbH
12489 Berlin, Germany

Prof. S. Raoux
Institut für Nanospektroskopie
Helmholtz-Zentrum Berlin für Materialien und Energie GmbH
12489 Berlin, Germany

Prof. S. Raoux
Institut für Physik
Humboldt-Universität zu Berlin
12489 Berlin, Germany

Keywords: perovskites, spatially-resolved photoemission, pin-holes, thin-film solar cells

The unprecedented speed at which the performance of solar cells based on solution processed perovskite thin films has increased, in some ways, appears to violate conventional understanding of device optimization. The relatively poor coverage of the TiO_2 electron transport layer by the absorber should cause shunting of the cell. This, however, is not the case. In this paper, it is attempted to explain this "discrepancy". Insights into coverage, morphology, local elemental composition, and spatially resolved electronic structure of $CH_3NH_3PbI_{(3-x)}Cl_x$ perovskite absorbers wet-chemically deposited on planar compact TiO_2 electron transport material (ETM) are revealed. Microscopy images indicate an incomplete coverage of the ETM. Depending on the degree of coverage, a variation in iodine oxidation and metallic lead formation is found. With the electronic structure of the absorber and the ETM established experimentally and taking literature on the commonly-used hole transport material spiro-MeOTAD into account, it is revealed that excellent charge selectivity occurs at the interfaces between the absorber and both the hole and electron transport layers. It can also be surmised that, crucially, any direct interface between the TiO_2 and spiro-MeOTAD would be characterized by a large recombination barrier preventing shunts; to some extent minimizing the negative effects of absorber pinholes.

1. Introduction

Solid-state hybrid solar cells using solution-processable organolead trihalide perovskite (AMX_3, with A = e.g., $CH_3NH_3^+$ or $CH(NH_2)_2^+$; M = e.g., Pb or Sn; and X = I, Cl, or Br) absorber layers have exceeded 20% conversion efficiency.[1-5] The highest efficiencies are achieved with a mesoporous electron transport material (ETM) scaffold of either TiO_2 or Al_2O_3 upon which the perovskite is spin-coated.[6] In principle, devices based on a simpler planar heterojunction configuration should also be capable of reaching high performances. Hence, significant efforts are aimed at developing a successful method to deposit the perovskite directly on compact ETMs such as TiO_2 (e.g., from solution at low process temperatures <150 ºC).[7-9] Spin-coating perovskite on planar ETMs tends to lead to incomplete coverage, limiting efficiency.[7] It has been reported that pin-hole formation in the perovskite layer may decrease light absorption (limiting the current) and create low-resistance shunt paths where the hole transport material (HTM) and the ETM may come in direct contact, creating electron-hole recombination paths (limiting the voltage).[10] Recently, a transparent, insulating, shunt-blocking layer preferentially deposited on the uncovered ETM was introduced into the device structure,[11] enhancing open circuit voltage without deteriorating charge extraction. For future optimization efforts, a comprehensive "spatially resolved" understanding of the chemical and electronic properties of the perovskite/ETM interface formation is crucial.

Studies investigating the chemical and electronic properties of interfaces found in perovskite-based solar devices are scarce.[12-17] This is particularly true for spatially resolved analysis. Here, we use scanning electron microscopy (SEM) and elemental distribution maps acquired by energy-dispersive x-ray spectroscopy (EDX) in combination with energy filtered photoemission electron microscopy (X-PEEM) to investigate the chemical and electronic properties of the interface formed between a $CH_3NH_3PbI_{(3-x)}Cl_x$ thin film wet-chemically deposited on a planar compact TiO_2 (c-TiO_2). SEM and EDX maps are used to gain insight into coverage, morphology, and local elemental composition; X-PEEM is used to study laterally-resolved chemical environment

with x-ray photoelectron spectroscopy (XPS) and x-ray absorption spectroscopy (XAS). These spatially resolved insights into the electronic structure at the $CH_3NH_3PbI_{(3-x)}Cl_x/TiO_2$ interface ultimately explain why perovskite absorbers with large pin-hole densities nevertheless result in working solar cells. Note that the impact of the morphology of similarly prepared $CH_3NH_3PbI_{(3-x)}Cl_x$ layers on c-TiO_2 on device performance was reported in detail in Ref. 7.

Despite the recent improvements in film morphology, creating ever more pinhole-free perovskite absorber layers, we expect the results (in particular related to the $CH_3NH_3PbI_{(3-x)}Cl_x/TiO_2$ interface) to be valid and crucial for the understanding and thus for the improvement of the solar cell device.

2. Results and Discussion

Morphology and elemental distribution

Figure 1a shows the SEM image of the surface of a nominal 300 nm thick $CH_3NH_3PbI_{(3-x)}Cl_x$ layer on c-TiO_2. The brighter areas show a perovskite film consisting of large grains – up to a few µm – which incompletely covers the c-TiO_2 substrate. The darker, small-grained areas are exposed c-TiO_2.[18]

The attribution of the different regions is further corroborated by the EDX elemental distribution maps shown in **Figure 1c-h**, derived from the same sample area as shown in Figure 1a. The substrate elements O, Sn, and Ti have the highest concentration in the darker areas of the SEM image, while I, Pb, and C have the highest concentration in the lighter areas. Thus, O, Sn, Ti and I, Pb, C are clearly anticorrelated; supporting the above conclusion that the perovskite does not completely cover the substrate. (See supplemental information, **Figure S1**, for the Cl K and N K fluorescence maps.).

The morphology observed in the PEEM image (**Figure 1b**) is similar to that in the SEM image (Figure 1a). The PEEM image of the perovskite/TiO_2 sample shows three distinct topographical regions, indicated in Figure 1b by differently colored rectangular boxes. The red box

indicates a region (hereafter called "perovskite") where the perovskite layer completely covers the TiO_2 substrate. The blue box indicates a sample area in which the perovskite layer seemingly does not cover the substrate, leaving the c-TiO_2 exposed (hereafter, "exposed TiO_2"). The area defined by the green box represents a sample area with a more complex ("intermediate") topography, showing a mixture of the areas described by the other two boxes. To study the chemical and electronic structure in these sample areas in detail (i.e., identify chemical species in addition to the element distribution given by the EDX maps), we employed local XAS and XPS spectroscopy enabled by PEEM.

Chemical speciation

PEEM-XAS was used to locally study the spatial distribution of Ti and relate it to the coverage of TiO_2 by the perovskite layer. Figure 2 shows the Ti $L_{2,3}$-edge XAS spectra of the perovskite sample recorded at the different areas of interest. For the "perovskite" area (red box in Figure 1b), no XAS Ti $L_{2,3}$-signal can be detected, indicating that the perovskite layer indeed completely covers the TiO_2 substrate in this area. The PEEM-XAS measurement is recorded in partial electron yield mode and thus the information depth is dominated by the inelastic mean free path (IMFP) of the detected photoelectrons. Taking into account that for the XAS measurements the electron analyzer is set to the kinetic energy of the secondary electrons (that induce maximum photoemission intensity) of only a few eV, we estimate the corresponding IMFP of these electrons, including multiple scattering in the material, based on the IMFP universal curve[19] to be in the range of around 3 nm. Considering that 95% of the exponentially attenuated signal comes from a "depth" of 3 × IMFP, it can be concluded that the perovskite layer in this specific sample area completely covers the compact TiO_2 with a minimal thickness of at least 9 nm (the nominal thickness is 300 nm).

The "exposed TiO_2" area that is indicated by the blue box in Figure 1b exhibits an intense Ti $L_{2,3}$ absorption signal that resembles the XAS spectrum of a TiO_2 anatase reference.[20] (The Ti $L_{2,3}$ XAS reference data of anatase has been digitized from Ref.[20] and is shown as the black spectrum

Figure 2. The PEEM-XAS data is shifted by 2.91 eV to higher photon energies for comparison. This shift could be due to energy miscalibration of the beamline.). The slight spectral differences can mainly be explained by the significantly lower energy resolution for the PEEM-XAS data. A clear Ti $L_{2,3}$-edge XAS spectrum can also be recorded from the "intermediate" sample area indicated by the green box in Figure 1b. The spectral shape – in a coarse comparison – also resembles the shape of the TiO_2 anatase reference; however, it is much less intense in comparison to the spectrum of the "exposed TiO_2" area. These results again indicate that the sample area defined by the green box in Figure 1b has a surface topography intermediate to that of the other two areas: in this "intermediate" sample area the substrate is partially covered by the perovskite layer, but the coverage is either incomplete or thin enough (i.e., < 9 nm) that a Ti $L_{2,3}$-signal from the exposed/underlying TiO_2 is still detectable.

For more information about the chemical environment of the perovskite layer and its spatially inhomogeneous interface with c-TiO_2, PEEM-XPS measurements were performed. **Figure 3** shows the I 4d XPS spectra of the three areas of interest defined in Figure 1b. The detailed analysis of the data can be found in S.I.; briefly, I 4d XPS signals (of varying intensity - note the magnification factors indicated on the right side of Figure 3) are detected in all regions of interest. For the "perovskite" and "intermediate" areas, the I 4d indicates the presence of one species (labeled component I in Figure 3). For the "exposed TiO_2" area, the data suggest (at least) two different chemical iodine species (components I and II in Figure 3). The main (I) contribution to the I $4d_{5/2}$ peak as measured in all regions can be ascribed to iodine in an iodide/perovskite environment (i.e., $CH_3NH_3PbI_3$). The assignment of the smaller I 4d (II) contribution (at higher BE) is difficult (see **Figure S2 and S3** and related discussion for more details), however, we tentatively attribute it to an iodite ($\rightarrow IO_2^-$) – type species. We caution that this assignment is speculative, because this compound is not stable (but exists as intermediate in iodide ↔ iodate reactions [21]). Furthermore, also the formation of a hypoiodite I^{+1} ($\rightarrow IO^-$) and/or an iodate I^{+3} ($\rightarrow IO_3^-$) species cannot be excluded (but is less likely– see S.I.). In conclusion, we will refer to this compound as "oxidized"

iodine species. Its presence could be explained by the formation of I-O_x bonds at the perovskite/TiO_2 interface. Its detection in the "exposed TiO_2" area can, however, only be understood by considering that before the crystallization annealing step the degree of coverage of the perovskite (precursor) layer on the compact TiO_2 is significantly larger.[13,22] As a result, some areas of the TiO_2 that have been covered with $CH_3NH_3PbI_{(3-x)}Cl_x$ pre-crystallization will then be exposed, revealing the remaining perovskite/iodite "seed layer". In the "exposed TiO_2" area, we derive a ratio of iodine species I:II (i.e., perovskite:"oxidized" iodine) of approximately 4:1. In the other areas the perovskite layer is too thick for surface sensitive XPS [inelastic mean free path (IMFP) for the I 4d photoelectrons excited with 120 eV is approximately 0.5 nm][23,24] to be able to probe the perovskite/TiO_2 region, and so species II is absent from these spectra. Note that the "effective" thickness (see S.I. for determination details) of the perovskite/iodite "seed layer" in the "exposed TiO_2" area is very thin; ca. 0.14 nm, which is smaller than the lattice constant of 0.64 nm and thus less than a monolayer of perovskite.[25]

Despite the rather large experimental BE uncertainty of ($\pm$ 0.2) eV, *relative* energy shifts have a significantly lower error bar and thus the BE shift of (0.3 $\pm$ 0.1) eV for the I 4d main contribution to higher BE values is small but significant. Taking into account that the I 4d intensity is significantly larger for the "perovskite" area (see the different magnification factors in Figure 3) – i.e., the $CH_3NH_3PbI_{(3-x)}Cl_x$ layer is thinner in the "exposed TiO_2" and "intermediate" sample area – the I 4d shift to higher BE might be explained by (interface induced) band bending. (For the sake of simplicity our model assumes a homogeneous coverage of the TiO_2 substrate.) Core level shifts to lower/higher BE indicate upwards/downwards band bending and thus the observed shift may suggest downward band bending towards the TiO_2. This effect would accelerate electrons towards the substrate and repel holes, which would benefit the perovskite/TiO_2 contact's charge selectivity.[26]

Figure 4 shows the results of the curve fit analysis of the Pb 4f XPS detail spectra of the examined areas. As with I, Pb is detected in all three regions of interest (see Figure 1b) but in

varying amounts (as denoted by the magnification factors on the right side of Figure 4). The BE of the Pb $4f_{7/2}$ peak recorded on the "exposed TiO_2" area (blue spectrum in Figure 4) is determined to be (138.61 ± 0.2) eV. There is only one Pb species found in this area. For the "perovskite" area (red spectrum in Figure 4), a single Pb species is also found with a Pb $4f_{7/2}$ BE of (138.34 ± 0.2) eV. The BE shift between the Pb 4f spectra of the "exposed TiO_2" and "perovskite" areas is in agreement with the shift observed in the I 4d spectra and can be (also) explained by interface induced band bending (see related discussion above). The Pb 4f XPS spectrum of the "intermediate" area (green spectra in Figure 4) clearly shows the presence of two different chemical Pb species. The Pb $4f_{7/2}$ peak of the main Pb contribution (I) is located at a BE of (138.66 ± 0.2) eV, whereas the second Pb contribution (II) is found at lower BE: (137.11 ± 0.2) eV. The Pb $4f_{7/2}$ line recorded for the "perovskite" and "exposed TiO_2" areas, and for the main Pb contribution (I) of the "intermediate" area is indicative for Pb in a perovskite.[27] The additional (minor) Pb contribution II (i.e., at low BE side) in the "intermediate" area (green spectra Figure 4) can be ascribed to metallic Pb. The composition ratio between the Pb species from the perovskite (I) and metallic Pb (II) is approximately 2:1.

Note that based on the presented I 4d and Pb 4f core levels, it is not possible to distinguish between $CH_3NH_3PbI_3$ and PbI_2, as the I- and Pb-related photoemission lines of both species have very similar BE.[28] Hence, the presence of PbI_2 cannot be excluded. In fact, the comparison of the different scaling factors given in Figure 3 and Figure 4 is actually (at least for one specific sample area) in agreement with the presence of PbI_2 as will be reasoned in the following. The ratio of the I 4d / Pb 4f scaling factors for the three different sample areas is (by definition) 1 / 1 for the "perovskite" area, 2.2 / 1.3 for the "intermediate" area, and 3.0 / 6.7 for the "exposed TiO_2". Note that the scaling factors were chosen such that the main contribution (I) of the respective photoemission line covers the same area. Since Pb 4f and I 4d have additional contributions (II) for the "intermediate" area and the "exposed TiO_2", respectively, the factor ratios are underestimated and overestimated in these cases. We find the I 4d / Pb 4f scaling factor ratio to be < 1 for the

"intermediate" sample area and to be > 1 for the "exposed TiO_2". Hence, relative to the I/Pb ratio of the "perovskite" area the "intermediate" sample area is I-poor or Pb-rich and the "exposed TiO_2" is I-rich or Pb-poor. While the former could be explained by the presence of PbI_2 in the "intermediate" sample area, the latter might indicate the diffusion/incorporation of (excess) iodine into the (upper region of the) TiO_2 substrate forming I-O_x bonds.

The latter is corroborated by the fact that I is a well-known dopant in TiO_2[29] with nominal doping levels up to 15 wt%.[30] The I–O–I and I–O–Ti bonds that are suggested to result from the incorporation of I into the TiO_2 structure [31] are so far in agreement with our results, as they are in line with the attribution of the high BE component (II) of the I 4d line to an "oxidized" I species (see discussion above and Figure 3). However, XPS data of I-doped TiO_2 usually show the dopant related photoemission lines at even higher BE values,[29-31] indicating that I is present in higher valencies than in our case. This indicates that instead of having a classical I-diffusion into the TiO_2, interfacial I-O_x bonds are formed upon $CH_3NH_3PbI_{(3-x)}Cl_x$ deposition by iodine incorporation in the upper c-TiO_2 region However, the presence of I-doped TiO_2 can also not be excluded.

The presence of metallic Pb has recently been related to x-ray induced degradation of the perovskite,[32] and metallic Pb and PbI_2 have been reported as products of degradation of $CH_3NH_3PbI_3$ in vacuum under visible light (24 h exposure).[33] In our experiment, all areas of interest on the sample are irradiated equally and simultaneously, but metallic Pb can only be identified in the "intermediate" area, and as described in the previous paragraph there is also some indication of PbI_2 formation in this area. This finding indicates that, if the formation of metallic Pb (possibly together with PbI_2) in vacuum is indeed a photon-induced effect, then it occurs (or starts) only locally, and it presumably is affected by laterally varying composition.

Lateral variation of the electronic structure

The 0 – 50 eV BE range, covering the valence band maximum (VBM) and shallow core levels (Ti 3p, O 2s, and Pb 5d), of the three regions of interest is depicted in **Figure 5** (see S.I. for a more

detailed analysis). The photoionization cross section for the Ti 3p line at this excitation energy is roughly one order of magnitude higher than that of the Pb 5d line,[34,35] which accounts for some of the intensity difference that can be observed and is reflected in the magnification factors. The VBM positions indicated in Figure 5 have been derived by linear extrapolation of the leading edge. The PEEM-XPS energy scale was calibrated by using an energy-calibrated data set measured at a different experimental setup, and so, also due to the low-signal-to noise ratio, only relative instead of absolute VBM positions are discussed below. The VBM of the "intermediate" and "perovskite" sample areas are shifted by (-0.2 ± 0.2) eV and (-1.7 ± 0.2) eV, respectively, with respect to the VBM of the "exposed TiO_2". The spectrum of the "intermediate" area is dominated by TiO_2 signals with minor contributions from Pb 5d (see Figure 5); hence the VBM position is also dominated by the O 2p states of TiO_2. The small VBM shift compared to the "exposed TiO_2" area is ascribed to some marginal spectral intensity near the Fermi level (E_F) – most likely caused by hybridized Pb 6s and I 5p states;[17] likely from the perovskite/iodite "seed layer." The low signal-to-noise ratio prevents a proper accounting for this low-intensity signal.

If the "exposed TiO_2" VBM – despite the fact that I- as well as Pb-related XPS signals have been identified in this sample area (see discussion above and Figure 3 and Figure S5) – is considered to represent the electronic structure of bare TiO_2, then the observed VBM shift with respect to the "perovskite" would approximate the VB offset (VBO) at the $CH_3NH_3PbI_{(3-x)}Cl_x/TiO_2$ interface. This assumption is somewhat justified by the significantly lower photoionization cross sections of the Pb- and I-derived compared to the O-derived VB states. However, in order to derive the true VBO, the observed VBM shift would have to be corrected for interface induced band bending (iibb). In any case, the VBM difference between the "perovskite" and the "exposed TiO_2" sample area of (-1.7 ± 0.2) eV is in good agreement with the value of -1.86 eV found by Schulz et al. for $CH_3NH_3PbI_{(3-x)}Cl_x$ and bare TiO_2.[14]

We can infer a complete energy level alignment of the $CH_3NH_3PbI_{(3-x)}Cl_x/TiO_2$ interface, including conduction band minima (CBM), from our measurements and literature data[14] (see S.I.

for more details). **Figure 6** shows this "zero-order" approximation (the "exposed TiO_2" data is assumed to represent the properties of the bare TiO_2 substrate, and any potential impact of iibb is neglected) suggests that a small negative (cliff-like) CB offset (CBO) is formed at the $CH_3NH_3PbI_{(3-x)}Cl_x/TiO_2$ interface. However, following the discussion related to Figure 3 and Figure S5, interpreting the (0.3 ± 0.1) eV shift of the I 4d and Pb 4f lines to higher BE values when going from the completely covered "perovskite" to the "exposed TiO_2" area indicating downward band bending in the perovskite towards the interface would result in a small positive (spike-like) CBO [i.e., CBM ($CH_3NH_3PbI_{(3-x)}Cl_x$) > CBM (TiO_2)]. Similarly, the VB difference of (-1.7 ± 0.2) eV would have to be iibb corrected, resulting in a true VBO of (-1.4 ± 0.2) eV. The CBO and VBO of the $CH_3NH_3PbI_{(3-x)}Cl_x/TiO_2$ layer stack would produce an ideal charge selective contact: The VBO is a sufficient barrier for holes; even more, the downward iibb towards the ETM TiO_2 will repel holes from, and accelerate electrons towards, the $CH_3NH_3PbI_{(3-x)}Cl_x/TiO_2$ interface. Even if a small spike-like CBO is formed, it is not expected to significantly hinder electron transport. Device simulations[36,37] for chalcopyrite-based solar cells have shown that a positive CBO of up to + (0.3 – 0.4) eV does not have any detrimental impact on device performance; in fact, a spike-like CBO will enlarge the interface band gap[38]: $E_{g,i}(CH_3NH_3PbI_{(3-x)}Cl_x/TiO_2) = E_{g,perovskite} + CBO = CBM_{TiO2}-VBM_{perovskite}$, which represents the (beneficial) energetic barrier for charge carrier recombination across the interface.

Why to (not) worry about pin-holes

To address whether pinholes in the perovskite on the ETM will limit efficiency[7] by creating low-resistance shunts where electrons and holes can recombine directly,[10] we compare our derived "exposed TiO_2" electronic structure to that of the most prominent HTM (spiro-MeOTAD). We align the energy level scheme for the spiro-MeOTAD surface found in Ref. [14] to our measurements using the reported relative shift between the VBM of $CH_3NH_3PbI_{(3-x)}Cl_x$ and the HOMO (highest occupied molecular orbital) of spiro-MeOTAD of 0.2 eV.[14]

In a zero-order approximation (i.e., neglecting any impact of band bending on the electronic structure of the spiro-MeOTAD/TiO_2 interface), **Figure 6** suggests significant (ca. 2 eV) energetic barriers between spiro-MeOTAD HOMO and TiO_2 VBM and between spiro-MeOTAD LUMO (lowest unoccupied molecular orbital) and TiO_2 CBM and thus would effectively prevent direct charge carrier transport between HTM and ETM.[39] Consequently, despite the formation of pinholes where the HTM and ETM can come in direct contact, perovskite-based solar cells deposited by e.g., spin-coating on planar TiO_2 still result in working solar cells. However, note that "real-world" interfaces are more complex. Imperfect lattices, grain boundaries, defects, and chemical interactions at the interface may very well also impact charge carrier recombination. In addition, the resulting interface band gap, i.e. $E_{g,i}$(spiro-MeOTAD/TiO_2) = CBM_{TiO2}-$HOMO_{spiro\text{-}MeOTAD}$ is presumably smaller than that discussed for the $CH_3NH_3PbI_{(3-x)}Cl_x$/TiO_2 interface above. Thus, we speculate that the rate/probability of charge carrier recombination at the spiro-MeOTAD/TiO_2 interface is enhanced, limiting the open circuit voltage of devices based on perovskite layers containing pin holes. This interpretation agrees with the observed improvement in open circuit voltage induced by a shunt-blocking layer.[11]

3. Conclusion

In summary, a combined SEM, EDX, PEEM-XPS and -XAS investigation of the surface of a 300 nm thick $CH_3NH_3PbI_{3-x}Cl_x$ layer deposited on (compact) TiO_2 FTO/glass shows an inhomogeneous morphology with an incomplete coverage of the substrate by the perovskite including holes that seemingly reach to the substrate. Spatially resolved XPS measurements reveal the presence of Pb and I in the "exposed TiO_2" area, which could not be resolved with EDX maps of the same sample type, suggesting the presence of perovskite remnants and/or the formation of a Pb-I(-O) containing seed/interface layer on the TiO_2 substrate. Additional indications of the formation of metallic Pb and an enhanced iodine-oxidation in the proximity of the perovskite/c-TiO_2 interface were observed. Depending on the degree of coverage, we find inhomogenous

chemical compositions of the absorber material, also reflected in the electronic structure. Combining the spatially-resolved VBM values determined from PEEM-XPS data with CBM values from literature, it was outlined that the energy level alignment at the HTM/perovskite and perovskite/ETM interfaces correlate to the performance level of respective solar cells. The HTM (here: spiro-MeOTAD)/perovskite and the perovskite/ETM (here: TiO_2) junctions represent (almost) ideal charge selective contacts for holes and electrons, respectively. Furthermore, the estimated energy level positions in the pin-hole areas, i.e. where the HTM and ETM are in direct contact, indicate a sufficient energetic barrier preventing high-rate charge carrier recombination and thus allowing solar cell devices to function even with high pin-hole densities.

4. Experimental Section

Sample preparation: Device-relevant $CH_3NH_3PbI_{(3-x)}Cl_x$ perovskite thin films of 300 nm nominal thickness were prepared on compact TiO_2/FTO/glass substrates at University of Oxford following the standard "one-pot" preparation approach.[6,8] The compact TiO_2 layers were spin-coated on fluorine-doped tin oxide (FTO) substrates (Pilkington, TEC7) by depositing an acidic solution of titanium isopropoxide dissolved in ethanol at 2000 rpm for 60s followed by drying at 150°C and annealing at 500°C for 45 min. The precursor solution for the perovskite was formed by dissolving methylammonium iodide (CH_3NH_3I, "MAI") and lead (II) chloride ($PbCl_2$) in anhydrous N,N-dimethylformamide (DMF) in a 3:1 molar ratio with a final concentration of 2.64 mol/l MAI and 0.88 mol/l $PbCl_2$. This solution was spin-coated onto compact TiO_2 at 2000 rpm in a nitrogen-filled glovebox for 45 s. After spin-coating, the films were left to dry at room temperature inside the glovebox to allow the solvent to slowly evaporate, followed by an annealing step for 2.5 h at 90°C (this step is needed for the crystallization and formation of the perovskite structure). After preparation, samples were sealed in a container under inert gas and transferred from the University of Oxford to the Helmholtz-Zentrum Berlin für Materialien und Energie, where they were unpacked and mounted on sample holders in a N_2-purged glovebox. During introduction of the samples into

the load lock of the X-PEEM endstation the samples were briefly (i.e., less than 2 min) exposed to air.

Scanning electron microscopy (SEM) and energy dispersive x-ray spectroscopy (EDX): SEM images of the sample surface were recorded using a commercially available Zeiss UltraPlus scanning electron microscope by measuring secondary electrons at a working distance of 47.8 mm and a primary electron beam acceleration voltage of 5 kV.

Energy dispersive x-ray spectroscopy (EDX) elemental distribution maps were acquired in the same microscope using an Oxford Instruments X-Max 80 X-ray detector and the AZtec acquisition and evaluation software. The beam energy and current were 7 keV and about 1 nA, respectively.

Note that SEM and/or EDX measurements recorded with an electron-beam energy of a few keV always risk being influenced (or, in the worst case, dominated) by artifacts due to beam-induced alteration of the material properties. This is particularly true for organic or inorganic/organic hybrid materials such as perovskites, as described in detail in Ref.[40]. The risks can be mitigated by limiting the exposure time of a particular area of the sample. Note that for the SEM and EDX data discussed in this paper, the comparison before and after measurements never showed visible changes in the morphology. Furthermore, no change of the elemental distribution of the surface (e.g., due to beam exposure-induced decomposition) was detected. Therefore, our measurements can be considered to be mainly free of electron beam induced artifacts, unless such deterioration occurs immediately at the beginning of the measurement.

Photoemission electron microscopy (PEEM): The PEEM characterization was performed in the Spectro-Microscope with Aberration correction for many Relevant Techniques (SMART) endstation installed at the UE49-PGM BESSY II beamline of the Helmholtz-Zentrum Berlin (HZB).[41,42] The UE49-PGM beamline offers an excitation energy range of 100 to 1200 eV. The SMART endstation is equipped with an imaging energy analyzer allowing for spatially resolved studies of samples (with in the best case) a maximal spatial resolution of 18 nm and an energy resolution of 180 meV

for X-PEEM.[43] All PEEM images have been recorded in a field of view of 12.4 µm.

The sample surface is imaged by recording photoemission from each point by means of a fluorescence screen in front of the imaging detector (here a CCD camera). For these PEEM topography images photon energy of 510 eV was used for excitation.

For the spectroscopy techniques (XPS, XAS) used within the microscopy mode, the electron energy resolution is realized by an energy filter (here an imaging energy analyzer) positioned in front of the detector. For visualization of the sample surface the contrast of each image is then determined according to the fulfillment of the energy conditions for a certain core electron (more details can be found in Refs. [41,42]). Briefly, the XPS measurements in microscopy mode (PEEM-XPS) are performed with a fixed photon energy by tuning the photoelectron kinetic energy detected by the analyzer through the energy range of interest. Spatially-resolved I 4d, Pb 4f, and extended valence band (i.e., shallow core level) XPS spectra were recorded in different areas of interest, using photon energies of 120, 380, and 200 eV, respectively.

XAS spectra in microscopy mode (PEEM-XAS) are recorded by setting the kinetic energy detected by the electron analyzer to the range of the secondary electron induced maximum photoemission intensity[41] and tuning the photon energy through the energy range of interest (i.e., the absorption edge). Thus, the XAS spectra are detected in partial electron yield mode. To measure the Ti $L_{2,3}$-edge XAS spectra, the photon energy was scanned from 450 to 470 eV.

Measured XPS peaks were fitted by using the fitting program "Fityk"[44] version 0.9.8. The binding energy (BE) of the core levels was determined by fitting a linear background and using Voigt profiles for the peaks. The fit parameters were constrained by fixing the area ratio of the spin-orbit doublets according to the multiplicity (2j+1) and coupling the peak shape and width for every core level of the same element and subshell. The spin-orbit splitting was fixed to 1.76 eV for the I $4d_{3/2}$ and $4d_{5/2}$ and to 4.86 eV for the Pb $4f_{5/2}$ and $4f_{7/2}$ levels.[45,46] The BE axis of the XPS data was calibrated by means of an energy-calibrated data set[12,13] measured at the High Kinetic Energy Photoelectron Spectrometer (HiKE) endstation installed at the KMC-1 beamline of BESSY II.[47,48]

The experimental BE uncertainty on an absolute energy scale is estimated to be (± 0.2) eV. However note that relative BE changes will have a significantly lower error bar.

As with electron beam irradiation, exposure to x-rays can also lead to measurement induced artifacts via degradation of the sample. However, similar to the SEM/EDX analysis for the data presented in this paper no indication for a modified sample morphology before and after accumulation of the PEEM data was observed. In addition, no spectral changes during XPS and XAS measurements were observed. However, x-ray-irradiation-induced changes on a shorter time-scale (i.e., any changes that occurred immediately upon irradiation) cannot be excluded.

Supporting Information
Supporting Information related to the EDX maps, the data evaluation of the I 4d and shallow core levels, as well as the energy level alignment is available from the Wiley Online Library.

Acknowledgements
We thank HZB for the allocation of synchrotron radiation beamtime for X-PEEM measurements. C.H. acknowledges support from the Potsdam University – HZB graduate school HyPerCells: Perovskites – Basic Research for High Efficiency Solar Cells. RF, EH, RGW, and MB additionally acknowledge funding from the Helmholtz Association (VH-NG- 423).

Received: ((will be filled in by the editorial staff))
Revised: ((will be filled in by the editorial staff))
Published online: ((will be filled in by the editorial staff))

References

[1] N. J. Jeon, J. H. Noh, W. S. Yang, Y. C. Kim, S. Ryu, J. Seo, S. I. Seok, *Nature* **2015**, *517*, 476.

[2] H. Zhou, Q. Chen, G. Li, S. Luo, T.-b. Song, H.-S. Duan, Z. Hong, J. You, Y. Liu, Y. Yang, *Science* **2014**, *345*, 542.

[3] W. Nie, H. Tsai, R. Asadpour, J.-C. Blancon, A. J. Neukirch, G. Gupta, J. J. Crochet, M. Chhowalla, S. Tretiak, M. A. Alam, H.-L.Wang, A. D. Mohite, *Science* **2015**, *347*, 522.

[4] W. S. Yang, J. H. Noh, N. J. Jeon, Y. C. Kim, S. Ryu, J. Seo, S. I. Seok, *Science* **2015**,

348, 1234.

[5] National Renewable Energy Laboratory (NREL), efficiency chart, https://www.nrel.gov/pv/assets/images/efficiency-chart.png, last accessed: June, 2017.

[6] M. M. Lee, J. Teuscher, T. Miyasaka, T. N. Murakami, H. J. Snaith, *Science* **2012**, *338*, 643.

[7] G. E. Eperon, V. M. Burlakov, P. Docampo, A. Goriely, H. J. Snaith, *Adv. Funct. Mater.* **2014**, *24*, 151.

[8] J. M. Ball, M. M. Lee, A. Hey, H. J. Snaith, *Energy Environ. Sci.* **2013**, *6*, 1739.

[9] H. J. Snaith, *J. Phys. Chem. Lett.* **2013**, *4*, 3623.

[10] M. Seetharaman, P. Nagarjuna, P. N. Kumar, S. P. Singh, M. Deepa, M. A. G. Namboothiry, *Phys. Chem. Chem. Phys.* **2014**, *16*, 24691.

[11] M. T. Hörantner, P. K. Nayak, S. Mukhopadhyay, K. Wojciechowski, C. Beck, D. McMeekin, B. Kamino, G. E. Eperon, H. J. Snaith, *Adv. Mater. Interfaces* **2016**, *3*, 1500837.

[12] D. E. Starr, G. Sadoughi, E. Handick, R. G. Wilks, J. H. Alsmeier, L. Köhler, M. Gorgoi, H. J. Snaith, M. Bär, *Energy Environ. Sci.* **2015**, *8*, 1609.

[13] G. Sadoughi, D. E. Starr, E. Handick, S. D. Stranks, M. Gorgoi, R. G. Wilks, M. Bär, H. J. Snaith, *ACS Appl. Mater. Interfaces* **2015**, *7*, 13440.

[14] P. Schulz, E. Edri, S. Kirmayer, G. Hodes, D. Cahen, A. Kahn, *Energy Environ. Sci.* **2014**, *7*, 1377.

[15] P. Schulz, L. L. Whittaker-Brooks, B. A. MacLeod, Dana C. Olson, Y.-L. Loo, A. Kahn, *Adv. Mater. Interfaces* **2015**, *2*, 1400532.

[16] E. M. Sanehira, B. J. Tremolet de Villers, P. Schulz, M. O. Reese, S. Ferrere, K. Zhu, L. Y. Lin, J. J. Berry, J. M. Luther, *ACS Energy Lett.* **2016**, *1*, 38.

[17] R. Lindblad, D. Bi, B.-w. Park, J. Oscarsson, M. Gorgoi, H. Siegbahn, M. Odelius, E. M. J. Johansson, H. Rensmo, *J. Phys. Chem. Lett.* **2014**, *5*, 648.

Formatiert: Englisch (USA)

[18] L. Huang, Z. Hu, G. Yue, J. Liu, X. Cui, J. Zhang, Y. Zhu, *Phys. Chem. Chem. Phys.* **2015**, *17*, 22015.

[19] W. S. M. Werner, *Surf. Interface Anal.* **2001**, *31*, 141.

[20] G. S. Henderson, X. Liu, M. E. Fleet, *Phys. Chem. Miner.* **2002**, *29*, 32.

[21] Y. K. Gupta, D. N. Sharma, *J. Phys. Chem.* **1971**, *75*, 2516.

[22] V. M. Burlakov, G. E. Eperon, H. J. Snaith, S. J. Chapman, A. Goriely, *Appl. Phys. Lett.* **2014**, *104*, 091602.

[23] S. Tougaard, *QUASES-IMFP-TPP2M*. 2002

[24] S. Tanuma, C. J. Powell, D. R. Penn, *Surf. Interface Anal.* **1994**, *21*, 165

[25] T. Oku, *Solar Cells – New Approaches and Reviews*, InTech, **2015,** Ch. 3.

[26] Y. Zhang, M. Liu, G. E. Eperon, T. C. Leijtens, D. McMeekin, M. Saliba, W. Zhang, M. de Bastiani, A. Petrozza, L. M. Herz, M. B. Johnston, H. Lin, H. J. Snaith, *Mater. Horiz.* **2015**, *2*, 315.

[27] National Institute of Standards and Technology, "NIST X-ray Photoelectron Spectroscopy (XPS) Database." [Online], Available: http://srdata.nist.gov/xps/Default.aspx

[28] Y. Li, X. Xu, Ch. Wang, C. Wang, F. Xie, J. Yang, Y. Gao, *AIP Adv.* **2015**, *5*, 097111.

[29] W. Su, Y. Zhang, Z. Li, L. Wu, X. Wang, J. Li, X. Fu, *Langmuir* **2008**, *24*, 3422.

[30] Q. Zhang, Y. Li, E. A. Ackerman, M. Gajdardziska-Josifovska, H. Li, *Appl. Catal., A* **2011**, *400*, 195.

[31] G. Liu, C. Sun, X. Yan, L. Cheng, Z. Chen, X. Wang, L. Wang, S. C. Smith, G. O. (M.) Lu, H.-M. Cheng, *J. Mater. Chem.* **2009**, *19*, 2822.

[32] B. Philippe, B.-W. Park, R. Lindblad, J. Oscarsson, S. Ahmadi, E. M. J. Johansson, H. Rensmo, *Chem. Mater.* **2015**, *27*, 1720.

[33] X. Tang, M. Brandl, B. May, I. Levchuk, Y. Hou, M. Richter, H. Chen, S. Chen, S. Kahmann, A. Osvet, F. Maier, H.-P. Steinrück, R. Hock, G. J. Matt, C. J. Brabec, *J. Mater. Chem. A* **2016**, *4*, 15896.

[34] M.B. Trzhaskovsaya, V. I. Nefedov, V. G. Yarzhemsky, *At. Data Nucl. Data Tables* **2001**, *77*, 97.

[35] M.B. Trzhaskovsaya, V. I. Nefedov, V. G. Yarzhemsky, *At. Data Nucl. Data Tables* **2002**, *82*, 257.

[36] T. Minemoto, T. Matsui, H. Takakura, Y. Hamakawa, T. Negami, Y. Hashimoto, T. Uenoyama, M. Kitagawa, *Sol. Energy Mater. Sol. Cells* **2001**, *67*, 83.

[37] X. Liu, J. R. Sites, *AIP Conf. Proc.* **1996**, *353*, 444.

[38] R. Scheer. *J. Appl. Phys.* **2009**, *105*, 104505.

[39] J. Krüger, U. Bach, M. Grätzel, *Adv. Mater.*, **2000**, *12*, 447.

[40] N. Klein-Kedem, D. Cahen, G. Hodes, *Acc. Chem. Res.* **2016**, *49*, 347.

[41] R. Fink, M. R. Weiss, E. Umbach, D. Preikszas, H. Rose, R. Spehr, P. Hartel, W. Engel, R. Degenhardt, R. Wichtendahl, H. Kuhlenbeck, W. Erlebach, K. Ihmann, R. Schlögl, H.-J. Freund, A. M. Bradshaw, G. Lilienkamp, Th. Schmidt, E. Bauer, G. Benner, *J. Electron Spectrosc. Relat. Phenom.* **1997**, *84*, 231.

[42] Th. Schmidt, U. Groh, R. Fink, E. Umbach, O. Schaff, W. Engel, B. Richter, H. Kuhlenbeck, R. Schlögl, H.-J. Freund, A. M. Bradshaw, D. Preikszas, P. Hartel, R. Spehr, H. Rose, G. Lilienkamp, E. Bauer, G. Benner, *Surf. Rev. Lett.* **2002**, *09*, 223

[43] Th. Schmidt, A. Sala, H. Marchetto, E. Umbach, H.-J. Freund, *Ultramicroscopy* **2013**, *126*, 23.

[44] M. Wojdyr, *J. Appl. Crystallogr.* **2010**, *43*, 1126. http://fityk.nieto.pl/

[45] L. Karlsson, S. Svensson, P. Baltzer, M. Carlsson-Göthe, M. P. Keane, A. Naves

de Brito, N. Correia, B. Wannberg, *J. Phys. B: At. Mol. Opt. Phys.* **1989,** *22*, 3001.

[46] J. F. Moulder, W. F. Stickle, P. E. Sobol, K. D. Bomben, J. Chastain. *Handbook of x-ray photoelectron spectroscopy: a reference book of standard spectra for identification and interpretation of XPS data.* Perkin-Elmer Corporation, Physical Electronics Division, Minnesota, USA, **1992**.

[47] M. Gorgoi, S. Svensson, F. Schäfers, G. Öhrwall, M. Mertin, P. Bressler, O. Karis, H. Siegbahn, A. Sandell, H. Rensmo, W. Doherty, C. Jung, W. Braun, W. Eberhardt, *Nucl. Instrum. Methods Phys. Res., Sect. A* **2009**, *601*, 48.

[48] F. Schaefers, M. Mertin, M. Gorgoi, *Rev. Sci. Instrum.*, **2007**, *78*, 123102.

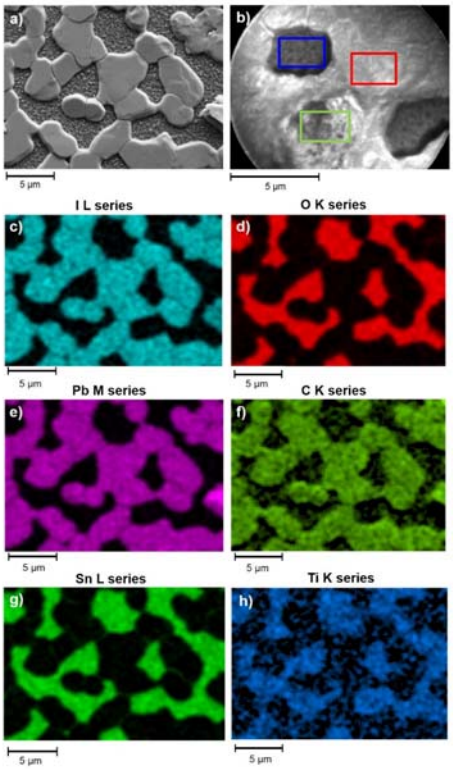

Figure 1. SEM (a) and PEEM (b) images of similarly prepared 300 nm thick $CH_3NH_3PbI_{(3-x)}Cl_x$ layers on compact TiO_2 on FTO/glass substrates**.** EDX maps of the iodine L (c), oxygen K (d), lead M (e), carbon K (f), tin L (g) and titanium K (h) fluorescence of the same sample spot as show in (a). **Different areas of interest are indicated in the PEEM image (b) by differently colored rectangular boxes.**

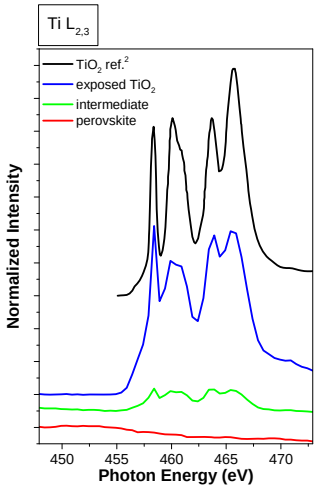

Figure 2. PEEM-XAS (shifted by 2.91 eV) spectra of the Ti $L_{2,3}$-edge recorded in the three different areas of interest defined in the PEEM image shown in Figure 1b of the nominal 300 nm thick perovskite layer on compact TiO_2: "exposed TiO_2" – blue box; "intermediate" area – green box; "perovskite" – red box. For comparison, a TiO_2 (anatase) reference spectrum from Ref.[20] is depicted.

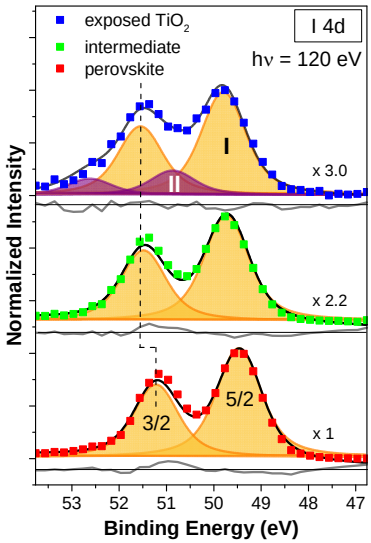

Figure 3. PEEM-XPS I 4d detail spectra (including fit analysis) of a nominal 300 nm thick perovskite/compact TiO_2 sample recorded in different areas of interest (as defined in the PEEM image shown in Figure 1b): "exposed TiO_2" – blue box; "intermediate" area – green box; "perovskite" – red box. Note the different magnification factors. The raw data is shown as solid squares; the resulting fits are given as black lines. The different contributions due to spin-orbit splitting and different iodine species are given as shaded areas in orange (species I) and purple (species II). The corresponding residual (i.e., the difference between data and fit) is shown below each spectrum. The spectral shift is indicated for the I $4d_{3/2}$ spin-orbit split main component with a vertical dashed line.

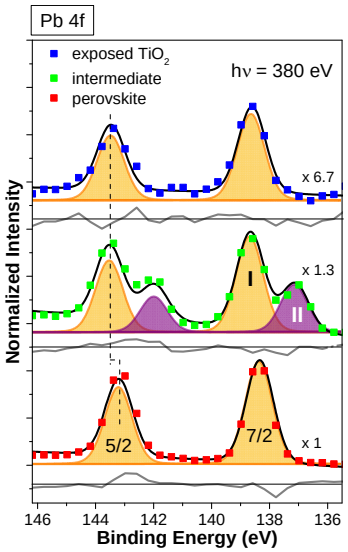

Figure 4. PEEM-XPS Pb 4f detail spectra (including fit analysis) recorded in different areas of interest (as defined in the PEEM image of Figure 1b) on the nominal 300 nm thick perovskite/compact TiO_2 sample: "exposed TiO_2" – blue box; "intermediate" area – green box; "perovskite" – red box. Note the different magnification factors. The raw data are shown as solid squares; the resulting fits are given as black lines. The different contributions due to spin-orbit splitting and different lead species are given as shaded areas in orange (species I) and purple (species II). The corresponding residual (i.e., the difference between data and fit) is shown below each spectrum. The spectral shift is indicated for the Pb $4f_{5/2}$ spin-orbit split component with a vertical dashed line.

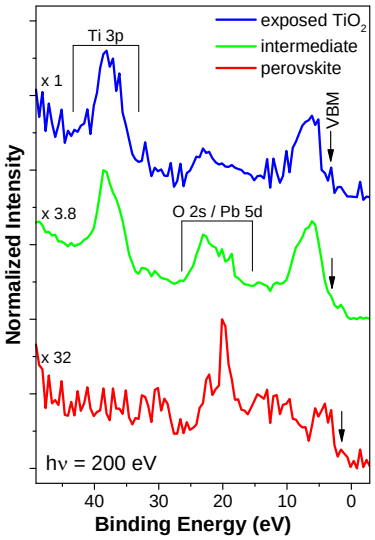

Figure 5. PEEM-XPS spectra of the shallow core levels and valence band region of the different areas of interest (as defined in the PEEM image of Figure 1b) on the 300 nm thick perovskite/compact TiO_2 sample: "exposed TiO_2" – blue box; "intermediate" area – green box; "perovskite" – red box. Note the different magnification factors. The shallow core level lines are labelled and the positions of the valence band maxima (VBM) are indicated by arrows.

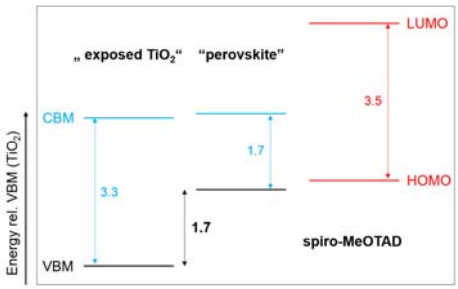

Figure 6. Schematic presentation of the relative difference between the PEEM-XPS derived VBM positions of the “exposed TiO_2” and “perovskite” sample area surface (black lines). The CBM positions (blue lines) were estimated by using the electronic band gap values for TiO_2 (3.3 eV) and $CH_3NH_3PbI_{(3-x)}Cl_x$ (1.7 eV) reported by Schulz et al.[14] For comparison of the electronic structure of a prominent ETM (TiO_2) with that of a prominent HTM (spiro-MeOTAD), the energy level scheme of a spiro-MeOTAD (red lines) was also taken from Ref. [14] and aligned according to the reported energy difference between the VBM position of $CH_3NH_3PbI_{(3-x)}Cl_x$ and the HOMO of spiro-MeOTAD. All values are given in eV and the experimental uncertainty of the stated VBM shift between the “exposed TiO_2” and “perovskite” sample area is ($\pm$ 0.2) eV.

Spatially resolved chemical and electronic structure investigations of $CH_3NH_3PbI_{(3-x)}Cl_x/TiO_2$ samples show an incomplete coverage and inhomogeneous properties. We find varying likelihood of iodine oxidation and metallic lead formation, an excellent charge selectivity at the contact interfaces, and a large recombination barrier between electron and hole transport layer, minimizing negative pinhole effects.

Keywords: perovskites, spatially-resolved photoemission, pin-holes, thin-film solar cells

Claudia Hartmann, Golnaz Sadoughi, Roberto Félix, Evelyn Handick, Hagen W. Klemm, Gina Peschel, Ewa Madej, Alexander B. Fuhrich, Xiaxia Liao, Simone Raoux, Daniel Abou-Ras, Dan Wargulski, Thomas Schmidt, Regan G. Wilks, Henry Snaith, and Marcus Bär**

Spatially-resolved insight into the chemical and electronic structure of solution processed perovskites – why to (not) worry about pin-holes

ToC figure ((Please choose one size: 55 mm broad × 50 mm high **or** 110 mm broad × 20 mm high. Please do not use any other dimensions))